

EEG 92129

Error bounds for EEG and MEG dipole source localization *

John C. Mosher^{a,c}, Michael E. Spencer^{a,b,c}, Richard M. Leahy^a
and Paul S. Lewis^b

^a *Signal and Image Processing Institute, University of Southern California, Los Angeles, CA 90089-2564 (USA)*, ^b *Los Alamos National Laboratory, MEE-3, Los Alamos, NM 87545 (USA)*, and ^c *TRW, Inc., One Space Park, Redondo Beach, CA 90278 (USA)*

(Accepted for publication: 21 December 1992)

Summary General formulas are presented for computing a lower bound on localization and moment error for electroencephalographic (EEG) or magnetoencephalographic (MEG) current source dipole models with arbitrary sensor array geometry. Specific EEG and MEG formulas are presented for multiple dipoles in a head model with 4 spherical shells. Localization error bounds are presented for both EEG and MEG for several different sensor configurations. Graphical error contours are presented for 127 sensors covering the upper hemisphere, for both 37 sensors and 127 sensors covering a smaller region, and for the standard 10–20 EEG sensor arrangement. Both 1- and 2-dipole cases were examined for all possible dipole orientations and locations within a head quadrant. The results show a strong dependence on absolute dipole location and orientation. The results also show that fusion of the EEG and MEG measurements into a combined model reduces the lower bound. A Monte Carlo simulation was performed to check the tightness of the bounds for a selected case. The simple head model, the low power noise and the few strong dipoles were all selected in this study as optimistic conditions to establish possibly fundamental resolution limits for any localization effort. Results, under these favorable assumptions, show comparable resolutions between the EEG and the MEG models, but accuracy for a single dipole, in either case, appears limited to several millimeters for a single time slice. The lower bounds increase markedly with just 2 dipoles. Observations are given to support the need for full spatiotemporal modeling to improve these lower bounds. All of the simulation results presented can easily be scaled to other instances of noise power and dipole intensity.

Key words: Spatiotemporal source modeling; EEG; MEG; Dipole source localization error; Dipole moment error

Electroencephalograms (EEGs) and magnetoencephalograms (MEGs) are non-invasive methods of studying the functional activity of the human brain with millisecond temporal resolution. Much of the work in EEG and MEG in the last few decades has been focused on estimating the properties of the internal sources of the fields from the external measurements (e.g., Snyder 1991). The most straightforward model for describing the surface evoked potential or the external evoked magnetic field is the single equivalent current dipole. In Mosher et al. (1992), we reviewed the many variations of this dipole model and its extensions to multiple dipoles and time epochs. Each of the

models, both in EEG and MEG, contains a transfer function or lead field model to relate each dipole's intensity, orientation, and location to the externally measured fields. The general inverse problem is to find the 3 location parameters and the 3 moment parameters that comprise the unknown parameters for each dipole.

The simplest head model in use is a set of homogeneous spherical shells, for which the MEG model is straightforward and the EEG model is still tractable, but with more parametric assumptions. Although a dipole comprises 6 parameters, the focus of most research has been on the accuracy of determining the 3 location parameters. Early studies compared the relative localizing ability of EEG and MEG (Cuffin and Cohen 1979; Cohen and Cuffin 1983). In Stok (1987), several of the model parameters were varied to determine which had the greatest impact on accuracy. In Cuffin (1990, 1991), the head shape and sphere models were examined for their accuracy impacts. In Cuffin (1986), variations of noise and measurement errors were explored for several array configurations. In Kaufman et al. (1991), the dipole source is expanded to

Correspondence to: Dr. R. Leahy, Signal and Image Processing Institute, University of Southern California, Los Angeles, CA 90089-2564 (USA).

* This work was supported by the Los Alamos National Laboratory, operated by the University of California for the United States Department of Energy under contract W-7405-ENG-36, by the TRW Doctoral Fellowship Program, and by the Kaprielian Innovative Research Fund at the University of Southern California.

a larger spatial extent to test the dipole assumption in cortical folds for both EEG and MEG models. In Achim et al. (1991) and Baumgartner et al. (1991), the spatiotemporal model was examined to determine its effectiveness in improving location accuracies.

The accuracies found and the conclusions drawn by these studies vary. Direct analysis of the localization error is complicated by the non-linearity of the location parameters, the sensitivity to the moment orientation, the moment intensity, the background noise power, the orientation and spatial extent of the sensors, and the absolute position of the dipole. Consequently, most of these studies and comparisons were restricted to specialized dipole locations or sensor positions. The error results were generally established by experimental data or by Monte Carlo analysis. More recently, dipoles implanted in patients have been used in an attempt to determine localization errors in MEG (Balish et al. 1991) and to compare localization errors between EEG and MEG (Cohen et al. 1990). The results of Cohen et al. (1990) have particularly led to recent controversy, with the study criticized on methodological grounds in Hari et al. (1991) and Williamson (1991). In *Therapeutics and Technology Assessment* (1992) and Anogianakis et al. (1992), the call is for careful consideration of the absolute accuracies of either modality under conditions that are fair to both modalities. As noted in Cohen and Cuffin (1983) and repeated in Anogianakis et al. (1992), EEG and MEG provide complementary data, and the use of both modalities can contribute to overall improved accuracy.

Our analysis of dipole localization error for MEG and EEG is based on the well-known Cramer-Rao Lower Bound (CRLB). The CRLB provides a lower bound on the variance of *any* unbiased estimator of the location and other model parameters. By deriving a closed-form expression for the bound, we can analyze for a much wider range of conditions than can studies based on Monte Carlo simulations or experimental data. The bounds are useful only if they are relatively tight (i.e., if they are not overly optimistic compared with the true localization error variances) and if the estimators employed have relatively small biases. To demonstrate the usefulness of the bounds, we present a Monte Carlo simulation which indicates that the CRLBs, in most cases, give reasonably accurate predictions of actual localization error variances. Preliminary results of this analysis were presented in Mosher et al. (1990).

We note that there are important limitations to this analysis, primarily due to the fact that the CRLB holds only under the assumption that the model is correct. The bounds give no insight into the effect of modeling error on localization accuracy. Nevertheless, in many of the cases shown, the CRLB gives surprisingly large lower bounds, even under fairly optimistic assump-

tions. Since modeling errors tend to degrade, rather than improve, performance, these results indicate that the accuracy of dipole localization based on single time epochs is often limited by the inherent ill-posed nature of the problem. The models analyzed here are some of the simplest in use. In general, more complicated models would be more prone to errors and could have more parameters to estimate. Consequently, the bounds presented here may pose fundamental limits on EEG and MEG localization performance.

In this paper, we present the Cramer-Rao lower bound for the general spatiotemporal model for an arbitrary number of sensors, an arbitrary number of time instances, and an arbitrary number of dipoles with arbitrary moments. We then present the specific formulas for the dipoles in a 4-shell sphere model for both the EEG and MEG case. These formulas are used in the subsequent sections to examine the lower bound on errors for several different array and dipole configurations. The localization error bounds are computed for one and two dipoles located in a plane in the upper hemisphere of the head. For each location, a search is performed over all possible dipole orientations to determine the best and worst results and the average localization error bounds. Graphical error contours are displayed for a quadrant in the upper-head hemisphere, providing rapid assessment and comparison of the two modalities.

Our emphasis is to present optimistic operating conditions with perfect models, many sensors, and low noise power, so that we may establish if the corresponding lower bounds indicate the potential for good dipole resolution. The use of identical sensor patterns allows, in each case, a cautious, but direct comparison of the differences in MEG and EEG source localization ability.

Forward models

We first discuss the general spatiotemporal model common to both EEG and MEG, then present EEG and MEG versions of the "dipole in a sphere" model, where sources are represented by current dipoles and the head is modeled as a concentric 4-shell sphere. This model illustrates how we adapt a specific EEG or MEG model to the general electromagnetic model, which in turn is used to determine the Cramer-Rao lower bounds.

The general model

By the superposition of electromagnetic sources, we can always separate the intensity of the sources as a linear term, whether we are considering these simple EEG and MEG spherical models or any other combi-

nation of head and source model. The vector of measured samples at time j can be modeled as

$$A(j) = \sum_{i=1}^p G(\vec{l}_i) \vec{q}_i = [G(\vec{l}_1) G(\vec{l}_2) \dots G(\vec{l}_p)] \begin{bmatrix} \vec{q}_1 \\ \vec{q}_2 \\ \dots \\ \vec{q}_p \end{bmatrix} = G(l)q(j) \quad (1)$$

where $A(j)$ is the column vector of surface potential or magnetic field measurements, or a combination of both. Column vectors l and q are both concatenations of the parameters for p dipoles, $l = [\vec{l}_1, \dots, \vec{l}_p]$ and $q = [\vec{q}_1, \dots, \vec{q}_p]^T$. The vector \vec{l}_i represents the 3-dimensional location of the i th current dipole, and \vec{q}_i represents the corresponding 3-dimensional dipole moment. The matrix $G(\vec{l}_i)$ represents the "gain transfer" matrix for the i th dipole, which relates the dipoles' moments to the vectors of measurements and has a non-linear dependence on the dipole locations.

For n time slices, we can extend this model by assuming that the dipole locations are fixed, yet allowing the dipole moments to vary with time:

$$A = [A(1), \dots, A(n)] = G(l)[q(1), \dots, q(n)] = G(l)Q. \quad (2)$$

We could also fix the dipole orientation over the time interval and factor out just the magnitude as a function of time, but for simplicity in this work we do not apply this restriction. In Mosher et al. (1992), details are presented that expand this representation for the "unconstrained," "rotating" and "fixed" orientation dipole models.

Concentric 4-sphere model for EEG

The EEG dipole model is the more complex of the two models, and assumptions must be made for the conductivities and shell thicknesses. The earliest models were for the dipole in a single homogeneous sphere (Wilson and Bayley 1950), which led to a closed form solution (Brody et al. 1973); however, this single sphere model is too simplistic because it does not model the relatively high resistivity of the skull layer. A concentric 3-sphere model that includes the scalp and skull layers was derived by Arthur and Geselowitz (1970). The 4-sphere model, which also accounts for the cerebrospinal fluid layer, was derived by Cuffin and Cohen (1979). Other models recently published include the eccentric 3-sphere model (Cuffin 1991) and the 4-sphere anisotropic model (Zhou and Van Oosterom 1992).

In this paper we use the concentric 4-sphere model. For a single dipole located at point \vec{l} , each element in (1) of the column vector of surface potential measurements represents the voltage at a single surface point \vec{p} and is expressed as the inner product of the (3×1) gain vector \vec{g}_v and the (3×1) dipole moment vector \vec{q} :

$$V(\vec{p}) = \vec{g}_v^T(\vec{l}, \vec{p}) \vec{q}. \quad (3)$$

where for clarity we show the dependence of the gain vector on both the dipole location and sensor position. The gain matrix $G(\vec{l})$ for a single dipole is the concatenation of the gain vectors for all sensor positions \vec{p} .

Fig. 1 shows the coordinate system used for the basic EEG formulas. For a dipole on the z -axis, the potential on the surface of the 4-sphere model referenced to infinity is given by Cuffin and Cohen (1979). Other dipole locations are found by applying rotation transformations to the basic formulas. We can express the gain vector for the 4-sphere model for arbitrary dipole position \vec{l} as

$$\vec{g}_v(\vec{l}, \vec{p}) = \sum_{n=1}^{\infty} w(n) \left(\frac{\|\vec{l}\|}{R} \right)^{n-1} [\vec{a}_{x'} P_n^1(\cos \theta') \cos \phi' + \vec{a}_{y'} P_n^1(\cos \theta') \sin \phi' + \vec{a}_{z'} n P_n(\cos \theta')] \quad (4)$$

where $P_n(\cdot) =$ Legendre polynomial of order n ; $P_n^1(\cdot) =$ associated Legendre polynomial; $R =$ outside radius of head sphere (in m); $\vec{a}_{x'}$, $\vec{a}_{y'}$, $\vec{a}_{z'}$ = basis for rotated coordinate axes that place the dipole on the z' -axis, i.e., $0 = \vec{a}_{x'}^T \vec{l}$, $0 = \vec{a}_{y'}^T \vec{l}$, and $\|\vec{l}\| = \vec{a}_{z'}^T \vec{l}$; θ' , ϕ' = polar coordinates of \vec{p} in the rotated system (Fig. 1).

The weighting function $w(n)$ in (4) is given by

$$w(n) = \left(\frac{1}{4\pi\gamma_4 R^2} \right) \frac{(2n+1)^4 (cd)^{2n+1}}{n\Gamma(n)} \quad (5)$$

where

$$\Gamma(n) = d^{2n+1} \{ b^{2n+1} n(k_1-1)(k_2-1)(n+1) + c^{2n+1} (k_1 n + n + 1)(k_2 n + n + 1) \cdot \{ (k_3 n + n + 1) + (n+1)(k_3-1)d^{2n+1} \} + (n+1)c^{2n+1} \{ b^{2n+1} (k_1-1)(k_2 n + k_2 + n) + c^{2n+1} (k_1 n + n + 1)(k_2-1) \} \cdot \{ n(k_3-1) + (k_3 n + k_3 + n)d^{2n+1} \} \quad (6)$$

$$k_1 = \frac{\gamma_1}{\gamma_2}, k_2 = \frac{\gamma_2}{\gamma_3}, k_3 = \frac{\gamma_3}{\gamma_4}, \quad (7)$$

and γ_1 , γ_2 , γ_3 , γ_4 are the conductivities of brain, cerebrospinal fluid, skull, and scalp, respectively, and b , c , d are the inner sphere radii normalized to the outer head sphere radius. Fig. 2 shows the 4 spheres with their respective radii and conductivities. Overlaid on the spheres are the sensor locations for the 37-channel pattern (one of the sensor arrays analyzed in this paper).

The formula for this EEG model explicitly shows that the voltage has a non-linear dependence on the dipole and electrode locations and a linear dependence on the dipole moment. The conductivities and radii shown were taken from Cuffin and Cohen (1979). We note that the relatively thin skull thickness, 4 mm in this case, gives favorable values for dipole localization; thicker skulls will produce higher error bounds. For example, Stok (1987) uses a skull thickness of 6 mm.

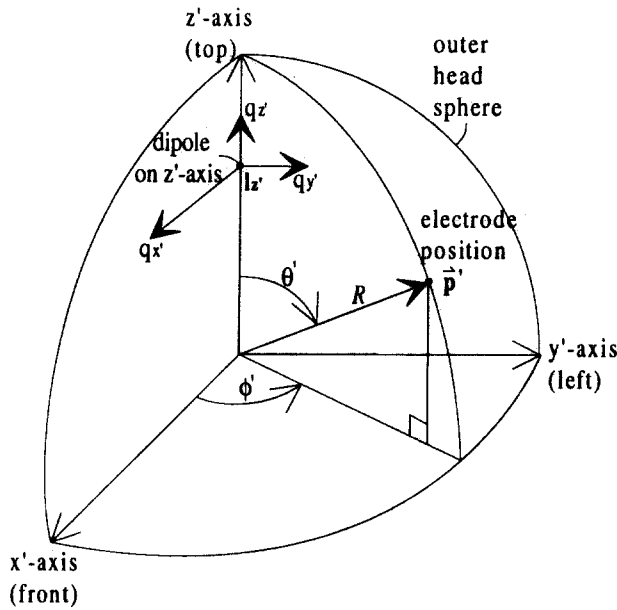


Fig. 1. EEG coordinate system for dipole on z-axis in a spherical head model. The EEG model generalizes to an arbitrary dipole location using standard coordinate transformations.

Biot-Savart law for MEG

Compared with its EEG counterpart, the MEG model for the dipole in a sphere with radially oriented sensors is quite simple. Radially oriented dipoles produce no magnetic field outside the concentric conducting spheres, regardless of the number of spheres we consider, and return volume currents produce no external magnetic fields in the radial direction. Sarvas (1987)

provides a thorough derivation of the general MEG formulas, then presents the simplifications that result for the spherically symmetric head model with radially oriented sensors.

For radially oriented sensors, the measured field is a relatively simple function of only the tangential components of the dipole moments. As noted by Ilmoniemi et al. (1985) and Sarvas (1987), the non-radial sensor orientations record magnetic fields that are also functions of only the tangential dipole moments, but the partials with respect to all of the parameters are not as simple as for the radial sensors. The restriction to the radial direction for sensor orientation is a common one; however, our approach makes it possible to study, directly, the question posed by Ilmoniemi et al. (1985) regarding the improvement gained for other sensor orientations.

We restrict ourselves to the radially oriented sensors, primarily for simplicity in presentation. This model has been published and extensively reviewed in the recent literature, and we present only a brief summary to clarify the terminology in relation to our model. The radially oriented MEG sensor coil is assumed to make a point measurement of the radial magnetic field. For a dipole located at \vec{l} , the scalar radial magnetic field $B(\vec{p})$ can be expressed as the inner product of gain vector \vec{g}_B and the dipole moment \vec{q} ,

$$B(\vec{p}) = \vec{g}_B^T(\vec{l}, \vec{p})\vec{q} \tag{8}$$

for sensor coil location \vec{p} . For the case of the spherical head model and the radial sensor measurements, this

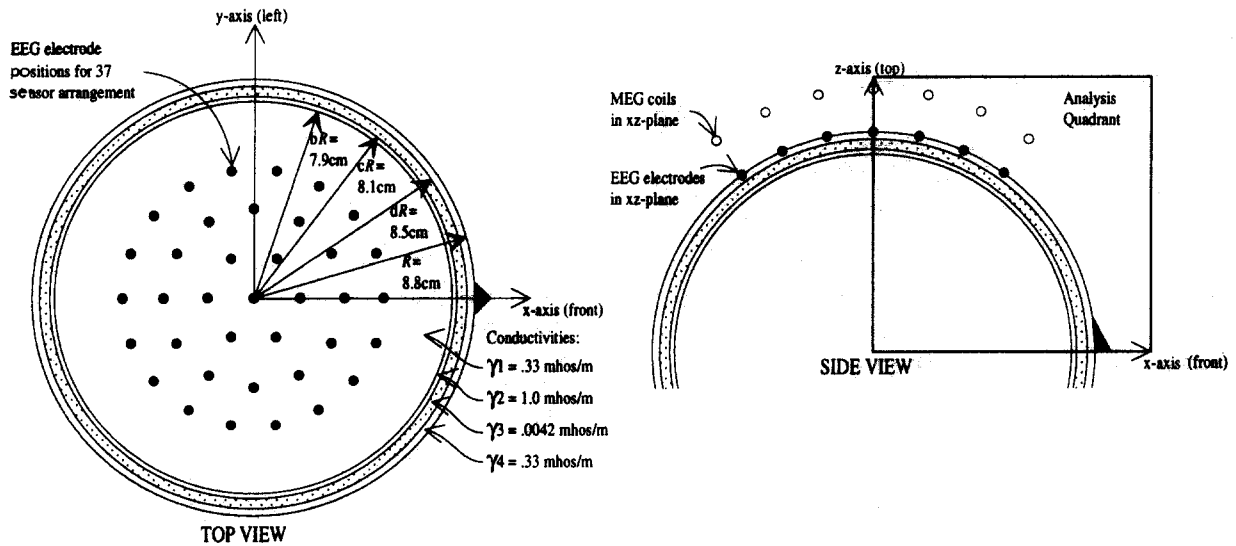


Fig. 2. Concentric 4-sphere model of head (Cuffin and Cohen 1979). The radii and conductivities are shown for the inner brain sphere, the cerebrospinal fluid layer, the skull layer (shaded), and the scalp layer. The EEG electrodes are located on the surface of the scalp at a radius of 8.8 cm; MEG coils are radially oriented 10.5 cm from the head center. For the 37-sensor case, the sensors are positioned in rings of 1, 6, 12, and 18 sensors each, separated by 12° as measured from the z-axis. The left figure shows the sensors as viewed from above. The right figure is the side view and shows the EEG electrodes and the MEG coils that lie in the x-z plane (y = 0) for the 37-sensor arrangements. The analysis quadrant shows where the CRLB bounds are computed relative to the head spheres and sensors.

gain vector is a special case of the Biot-Savart law and can be expressed as

$$\vec{g}_B(\vec{l}, \vec{p}) = \left(\frac{\mu_0}{4\pi}\right) \frac{(\hat{f} \times \vec{l})}{\|\vec{p} - \vec{l}\|^3} \quad (9)$$

where the coordinate system is assumed to be head centered and \hat{f} = unit radial orientation of the sensor coil, $\vec{p}/\|\vec{p}\|$; μ_0 = permeability of free space = $4\pi \times 10^{-7}$ (Vs/(Am)), and “ \times ” denotes the vector cross-product. The MEG gain matrix $G(\vec{l})$ for a single dipole is the concatenation of all gain vectors for all sensor locations.

Cramer-Rao lower error bound

The Cramer-Rao lower bound (CRLB) (e.g., Sorenson 1985) is an important result in estimation theory that establishes a lower bound on the variance of any unbiased estimator of a set of unknown parameters. Determining the bound requires a joint probability density function for the data. The existence of an unbiased estimator that attains the bound is not guaranteed. To demonstrate that these bounds are meaningful in this application, we need to show that (a) the estimators we use are effectively unbiased, and (b) the bounds are relatively tight, i.e., that the lower bound on the variance is close to the true attainable variance with a given estimator. To investigate the utility of the CRLB, we performed Monte Carlo studies using non-linear least-squares for localization. The results of this study are reported in “Monte Carlo Simulation.”

Fisher information matrix

Consider a set of data F , which we model as $F = G(I)Q + N$, where N is the unknown noise and $G(I)Q$ is the noiseless deterministic data. We assume that the locations I and the orientations and magnitudes Q of the dipole moments are unknown. We also assume that the noise N is zero-mean, spatially and temporally white, and normally distributed, and that it has an unknown variance ν . For convenience, we group these parameters into one vector ψ ,

$$\psi = \left[\nu, q(1)^T, \dots, q(n)^T, \vec{l}_1^T, \dots, \vec{l}_p^T \right]^T, \quad (10)$$

where each moment vector at each time instance j is the concatenation of the individual moments for each dipole, as

$$q(j)^T = [\vec{q}_1^T(j), \dots, \vec{q}_p^T(j)]. \quad (11)$$

Cramer-Rao inequality theorem. Let $\hat{\psi}$ be any unbiased estimate of the deterministic parameters in $F = G(I)Q + N$. Then the covariance matrix C of the errors between the actual and estimated parameters is bounded from below by the inverse of J , as

$$C = E\{(\psi - \hat{\psi})(\psi - \hat{\psi})^T\} \geq J^{-1} \quad (12)$$

where J is the Fisher Information Matrix

$$J = E\left\{ \left[\frac{\partial}{\partial \psi} \log p(F|\psi) \right] \left[\frac{\partial}{\partial \psi} \log p(F|\psi) \right]^T \right\}. \quad (13)$$

$E\{\}$ denotes the expected value or mean of the enclosed term, and $p(F|\psi)$ denotes the probability density function for the data given parameters ψ .

See Sorenson (1985) for a proof of this result. The inequality in (12) states that the difference matrix $(C - J^{-1})$ is positive semi-definite, and as a consequence, the variance of each parameter ψ_i is individually bounded by the corresponding diagonal element in J^{-1} . Under the assumption that the noise is spatially and temporally white and normally distributed, a closed form expression for (12) is possible. In the Appendix, we derive this result for the case of m sensors, n time instances, and p dipoles, in a general form that is applicable to both EEG and MEG data.

The Fisher Information Matrix and its inverse in the Appendix provide insight into how each parameter affects the estimate of the other parameters. Repeating (23) from the Appendix, for m sensors, n time slices, and variance ν , and with G , Δ and Γ defined in the Appendix, the Fisher Information Matrix is

$$J = \frac{1}{\nu} \begin{bmatrix} \left[\frac{mn}{2\nu} \right] & 0 & 0 \\ 0 & \mathbf{I}_n \otimes G^T G & \underline{\Delta} \\ 0 & \underline{\Delta}^T & \Gamma \end{bmatrix}. \quad (14)$$

The upper left diagonal term in J , $(mn)/(2\nu)$, represents the information for the estimate of the noise power. The other entries in the first column and first row represent the cross-information between the noise power and the other parameters of our model, namely the moments and locations of the dipoles; these off-diagonal elements are zero. The CRLB requires that this matrix be inverted, and these zeros allow us to partition the matrix into two separate submatrices and invert them separately. Thus, the noise variance submatrix cannot affect the parameters in the other submatrix. Of course, the other lower bounds depend on the noise variance (there is a scalar noise variance term leading the matrix), but whether or not we assume that we know the noise variance is irrelevant, because the submatrix inversion to calculate the moment and location lower bounds is the same whether we *estimate* the noise variance or *assume* it.

In contrast, the lower bounds on either the set of moment parameters or the set of location parameters depend on whether we estimate both sets of parameters or assume one set known. We represent the information for the moments and the locations in the lower right submatrix in (14). The cross-information between the moments and the locations is represented by the off-diagonal term Δ . If we assume perfect knowledge

of the moments, then the CRLB of the locations would reduce to the first bracketed term in (25). Similarly, if the locations are perfectly known, the CRLB for the moments would reduce to the first bracketed term in (30). In the general dipole localization problem, we know neither the moment nor the location, and the second term in each of these CRLB equations shows that we cannot simply ignore the cross-information term Δ . This cross-coupling will generally increase the error lower bounds. Thus, consideration of the estimation of both the moment and the location is critical for lower bound accuracy.

Location error lower bounds

Equations (24), (29) and (30) in the Appendix are for the general multiple dipole spatiotemporal model. They express the lower bound for the variance, the dipole location, and the dipole moment. Our approach in this paper is to focus on the variance of the dipole location error, since much MEG and EEG work emphasizes the ability or inability of the different modalities to locate the source of neural activity. To gain insight into the utility of the formulas and establish some basic lower bounds, in the Appendix we simplify the formulas for the case of a single time slice and multiple dipole sources of equal scalar intensity Q . In this case, the scalar Q factors out and can be grouped with the variance of the noise. Repeating (32) from the Appendix,

$$\text{CRLB}(\mathbf{l}) = \frac{\nu}{Q^2} \left[(\mathbf{D}\hat{\mathbf{X}})^T \mathbf{P}_G^\perp (\mathbf{D}\hat{\mathbf{X}}) \right]^{-1} \quad (15)$$

where $\text{CRLB}(\cdot)$ denotes the Cramer-Rao lower bound on the error covariance matrix of the enclosed vector, and ν is the variance of the additive gaussian noise. The matrices \mathbf{D} , $\hat{\mathbf{X}}$, and \mathbf{P}_G^\perp are explicitly defined in the Appendix, but broadly speaking, \mathbf{D} represents the matrix of partial derivatives of the gain transformation with respect to the locations, $\hat{\mathbf{X}}$ represents the moment orientations scaled to unity, and \mathbf{P}_G^\perp is a projection operator onto the orthogonal complement of the column space of the gain matrix \mathbf{G} . Eq. (15) illustrates how the dipole intensity and the noise variance can be lumped into a single scalar ratio of the two values, ν/Q^2 , and that the moment orientation can be isolated into a single term $\hat{\mathbf{X}}$. We can therefore easily scale our results for any desired noise power and moment intensity levels.

Best, average, and worst dipole orientation

For one dipole, the lower bound error analysis for EEG generates a 7×7 covariance matrix: 1 dimension for the noise variance, 3 dimensions for the moment, and 3 dimensions for the location. In the case of MEG, we only have 2 dimensions of the moment we can estimate, but in either case we always have 3 dimen-

sions assigned to the location. If we use cartesian coordinates for our location parameters, then the difference vector between our estimate of the location and the true location can be written as

$$\text{Location Error Vector} = [(x - \hat{x}), (y - \hat{y}), (z - \hat{z})]. \quad (16)$$

The corresponding 3×3 submatrix bounding the error covariance for these parameters would be

$$\text{CRLB}(\bar{\mathbf{l}}) = \begin{bmatrix} \sigma_{xx}^2 & \sigma_{xy}^2 & \sigma_{xz}^2 \\ \sigma_{xy}^2 & \sigma_{yy}^2 & \sigma_{yz}^2 \\ \sigma_{xz}^2 & \sigma_{yz}^2 & \sigma_{zz}^2 \end{bmatrix}. \quad (17)$$

Independent of our choice of coordinate systems, this bounding matrix can be represented by an error ellipsoid. The major axes of the ellipsoid are found as the eigenvectors of the bounding matrix. The lengths of the axes are determined from the corresponding eigenvalues. The eccentricity of the ellipsoid indicates the directional bias that the error vectors will exhibit. Indeed, the minor axes of the ellipsoid represent the "preferred directions" discussed in Cohen and Cuffin (1983). If we consider the errors in any direction to be equally important, then we can ignore this directional bias and, instead, focus on the scalar length of this error vector. The lower bound on the expressed squared value of this length is the sum of the eigenvalues, or equivalently, the trace (sum of the diagonal elements) of the bounding matrix. Hence, at a given location $\bar{\mathbf{l}}$ and for a given moment $\bar{\mathbf{q}}$, we can define our scalar localization error bound in cartesian coordinates as

$$\text{RMS Location Error: } \sigma_l(\bar{\mathbf{l}}, \bar{\mathbf{q}}) = (\sigma_{xx}^2 + \sigma_{yy}^2 + \sigma_{zz}^2)^{1/2} \quad (18)$$

which, physically interpreted, is the lower bound on the root mean square (RMS) length of the 3-dimensional error vector given by (16).

We emphasize in (18) the dependency of this calculation on the moment of the dipole; different moment directions at the same location will generate, in general, different error ellipsoids. Since radial sources represent "silent sources" for MEG data, we have largely restricted our examination to sources lying in the tangential plane for both MEG and EEG data. This restriction also simplifies our analysis of the RMS location error, because the moment orientation can now be parameterized by the single parameter θ describing the angle the moment makes in the tangential plane.

For a given point $\bar{\mathbf{l}}$, we can "scan" over all possible θ , observing the RMS location error. Fig. 3 presents such a scan for two different sensor configurations. We see a strong dependency on the dipole orientation for one situation and relatively little dependency for the other. We retain 3 values from these curves: the best (lowest) RMS error, the worst, and the average over all angles. We illustrate in the examples to follow the

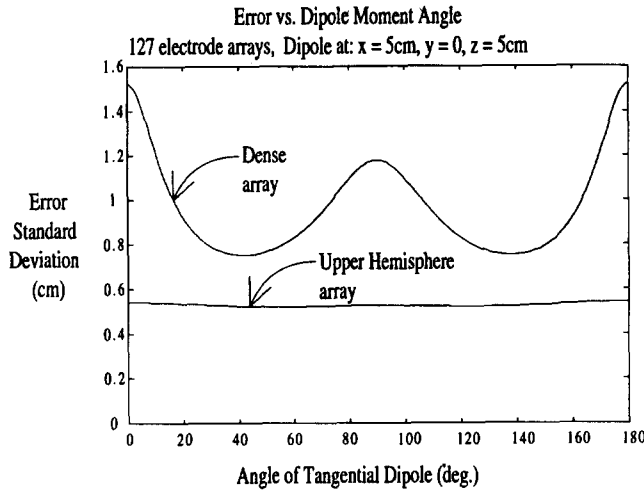


Fig. 3. RMS location error as a function of moment orientation angle. The moment direction was restricted to the tangential plane, because radial moments represent blind sources for MEG sensors. For each θ , the RMS location error is calculated using (18). This figure shows a comparison between two different sensor arrays for the same dipole location. The upper curve is for the dense 127-sensor pattern (see Fig. 7 for description), which is relatively more sensitive to the moment orientation, versus the lower curve for the 127 upper-hemisphere pattern (Fig. 5), which is insensitive to moment orientation. We retain 3 values from the curves: the best (lowest) error, the worst, and the average over all θ .

sensitivity of some sensor patterns to dipole orientation.

For 2 dipoles, we extend the above approach. Since 2 dipoles represent 6 location parameters, we have a 6-dimensional bounding matrix that represents all of the correlations between the parameters. If we focus on the error vectors that extend from the true locations to the estimated locations, we can still interpret the sum of the first 3 diagonal terms as the lower bound on the mean square error for the localization of the first dipole. The complexity is that *each* RMS error length depends on *both* dipole moments and *both* locations. We can express these RMS values using the 6 diagonal terms of the bounding matrix, expressed here in cartesian coordinates as

$$\begin{aligned}\sigma_{\vec{l}_1}(\vec{l}_1, \vec{q}_1, \vec{l}_2, \vec{q}_2) &= (\sigma_{x_1x_1}^2 + \sigma_{y_1y_1}^2 + \sigma_{z_1z_1}^2)^{1/2} \\ \sigma_{\vec{l}_2}(\vec{l}_1, \vec{q}_1, \vec{l}_2, \vec{q}_2) &= (\sigma_{x_2x_2}^2 + \sigma_{y_2y_2}^2 + \sigma_{z_2z_2}^2)^{1/2}.\end{aligned}\quad (19)$$

If we again restrict the moments of both dipoles so that they lie only in the tangential plane, we can parameterize these scalars as functions of angles for *each* moment. For a given pair of dipole locations, (\vec{l}_1, \vec{l}_2) , we scan over all possible combinations of θ_1 and θ_2 and again find the best, worst, and average RMS lengths for each dipole. In general, the best orientation occurs when the two moments are arranged orthogonally, so that the peak intensities of the dipoles are well separated in the field array. The worst ar-

rangement is for both dipoles to be aligned in the same direction, so that their intensity peaks coincide.

Monte Carlo simulation

All of the results presented in this paper represent the lower bound on the variance of the estimated location parameters for any unbiased estimator. In this section, we present the results of a Monte Carlo simulation based on a standard least-squares estimator for a 37-sensor MEG instrument. The full CRLB analysis assumptions are presented in the section on EEG and MEG Analysis Examples, and the specific details of the 37 sensor arrangement are presented in Thirty-seven-Sensor Pattern Results. We present the Monte Carlo results both to confirm the formulas and to demonstrate the closeness of the CRLBs to the actual RMS error results from our Monte Carlo study.

For each point on a 5 mm grid in a selected region of the upper positive quadrant of the x-z plane, we positioned a dipole in the best moment orientation as found by our CRLB analysis. We synthesized the single dipole forward model across the array using the same dipole intensity as in the analysis. For each grid point, we ran 5000 realizations of zero mean white gaussian noise at the sensors, using a random number generator with the same standard deviation as that used in the analysis. For each noise realization, we estimated the dipole location parameters using the Nelder-Meade nonlinear least-squares approach described in Mosher et al. (1992). We initiated the search within a 10 mm region around the true location to enhance the possibility of finding the global minimum and to avoid converging, instead, into a local minimum.

From these trials, we calculated the mean and RMS location error at each grid point. The mean location error for 95% of these grid points was less than 0.07 mm. This indicates that the non-linear least-squares estimator is effectively unbiased for this single dipole case. The RMS location errors were observed to be greater than or equal to the CRLBs, within normal experimental variation. We then continued the Monte Carlo analysis for a larger region in the upper head quadrant, restricting our repetitions to 100 trials per grid point. Fig. 4 presents the RMS location errors and the corresponding CRLB results. In all regions where the anticipated standard deviation is less than a few centimeters, we see excellent agreement between the Monte Carlo and CRLB results. The overall result is a confirmation of both the MEG CRLB formulas and evidence that the least-squares estimator comes very close to meeting the CRLB.

At a 5 mm spacing, the MEG Monte Carlo simulations here required many days of computation on a Sun SPARCstation 2 computer, because each of the

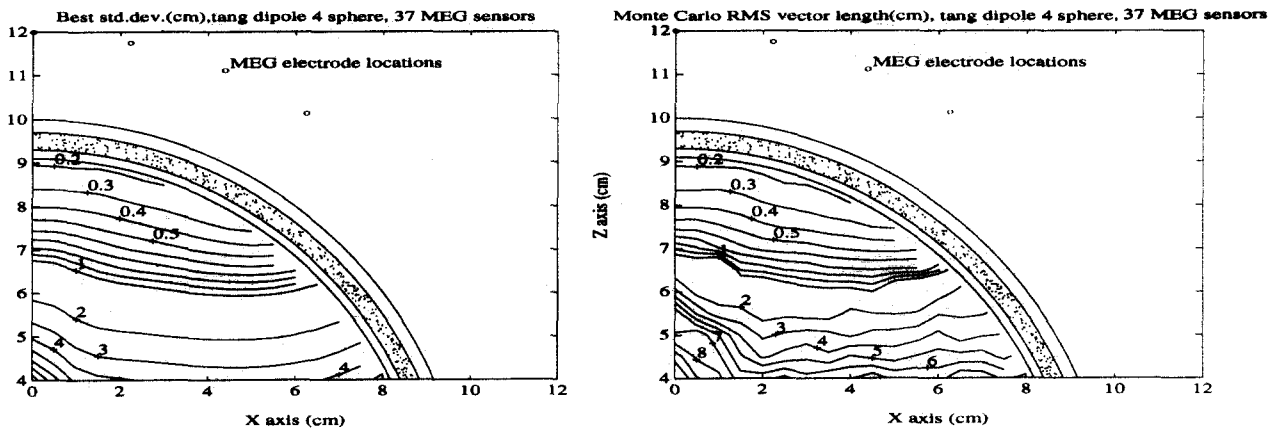


Fig. 4. Monte Carlo simulation and comparison. The left figure shows the computed CRLBs for a single dipole in a 37-channel MEG system. The right figure is the result of a 100-trial Monte Carlo simulation at each point in a 5 mm grid, using the same dipole intensity and noise variance as was used in the CRLB analysis. In deep regions, the signal received at the array is much weaker than the additive noise, and the Monte Carlo runs experienced difficulty converging. In the shallow head regions, the signal at the array is improved, and we see excellent agreement between the analysis and simulation.

error trials could require many hundreds of calls to the generating function, and because at each point in the grid, we perform 100 or 5000 trials. The equivalent EEG model would require an order of magnitude greater processing time, because of the greater complexity of its gain transfer function. This computational burden for a single Monte Carlo study, with a single dipole orientation, underscores the utility of the CRLB calculations in more rapidly assessing many sensor arrangements and all dipole orientations.

EEG and MEG analysis examples

The formulas presented above for the dipole in a concentric 4-sphere model are the general formulas for arbitrary sphere radii, tissue and skull conductivities, sensor and dipole locations, and dipole intensities and orientations. The CRLB formulas presented in the Appendix also apply for the general spatiotemporal model. Here, we restrict our numerical analysis to a few relatively simple cases of symmetric array patterns and one or two dipoles. The CRLB formulas require that the partial derivatives of the gain matrix with respect to the unknown location parameters also be calculated. The tedious calculations for the EEG model were carried out by hand, and verified using Maple V, a symbolic algebra computer program. The MEG partials were straightforward.

Analysis region

Fig. 2 displays one of the array patterns used here with relation to the spherical model. The other patterns were similarly symmetric about the z-axis, which runs through the center of the array. Because of this high degree of symmetry, we restrict our analysis region to the positive x-z plane. The error results in this

plane can then be inferred by symmetry for the entire upper hemisphere. As this analysis plane is rotated about the z-axis, differences will arise because of the finite spacing of the sensors; however, these differences are not anticipated to be great.

Dipole orientation

One of our goals in this study was to allow careful and cautious comparisons between EEG and MEG data. For the simple dipole in a sphere model used here, the radially oriented dipole generates no external magnetic field, so EEG holds an obvious advantage. We therefore restricted the orientation of the dipole to lie in the tangential plane for both the EEG and MEG data for most of the following error analyses. This restriction also simplified the parameterization of the dipole orientation to the single parameter θ , the angle the moment makes in the tangential plane. We note that this is not unduly restrictive, since all of the results presented here scale with dipole intensity Q . In the case of MEG data, a dipole with a radial component and an intensity Q would simply project into the tangential plane as a dipole with intensity $Q \cos \phi$, where ϕ is the angle made by the dipole with respect to the tangential plane. All of the standard deviations for the MEG data presented here could then be appropriately scaled to include any desired radial component. For comparison we also present some EEG results in which we place no restriction on the dipole moment orientation; the results are similar to those from the tangential dipole study.

Dipole intensity

The bounds presented in (15) could be normalized to the ratio ν/Q^2 , but these units of sensor noise variance ν to dipole intensity Q are non-intuitive and give the user no relative feel for the absolute localiza-

tion error. We therefore attempt to establish some realistic values for the dipole intensity, and in the next section, the noise variance. We note that this ratio can be viewed as a signal-to-noise ratio, defined here as $\text{SNR}(\text{dipole}) = Q/\sigma$, where σ is the standard deviation. By fixing the dipole intensity at Q , then moving this dipole about the upper hemisphere, the actual signal intensity received by the sensor array will vary, roughly, as the inverse function of the squared distance to the array. Hence, if we consider a second definition, $\text{SNR}(\text{array})$, to be a function of the signal at the array (either an average across all sensors or at the peak field among all sensors), then we observe that $\text{SNR}(\text{array})$ will drop as the dipole is moved deeper. Maintaining the $\text{SNR}(\text{array})$ as a constant over all dipole locations requires deeper dipoles to have correspondingly stronger intensities.

Variations of $\text{SNR}(\text{array})$ are common definitions in other studies (Cuffin and Cohen 1979; Cuffin 1986; Mosher et al. 1990; Oshiro et al. 1992), in which it is therefore not necessary to assign explicit units of amps to the dipole current. In such studies, all of the calculations are carried out in "relative units," where the signal at the array is set to one unit and the noise standard deviation is set to some ratio of this unit, for instance, 10%. We argue that the alternative $\text{SNR}(\text{dipole})$ is the preferred definition when the intent is to study the location error for a dipole or sets of dipoles arbitrarily located in the head. For $\text{SNR}(\text{array})$, adjusting the dipole intensity as a function of location will lead to distorted comparisons between different array configurations, because dipole intensity implicitly becomes a function of sensor location, and, in this study, a function of sensor type (EEG or MEG). Deeper dipoles may also be assigned unrealistically high currents simply to keep the $\text{SNR}(\text{array})$ constant. A fixed dipole intensity at a physically plausible current leads to a more informative accuracy analysis and to more direct comparisons between configurations.

In Cohen and Cuffin (1983), a relatively strong dipole was estimated to have a dipole intensity of $2.1 \mu\text{A}\cdot\text{cm}$ (21 nA-m). In Cohen et al. (1990), an implanted dipole of 16 mm length was stimulated with $4 \mu\text{A}$ current, for an equivalent 64 nA-m current dipole. We wished to establish a baseline dipole intensity of the proper order of magnitude that was readily scaled to other intensities, and that appeared physically plausible. We selected 10 nA-m as our dipole intensity. With this selection, we can present accuracy bounds in units of meters, but we emphasize, however, that all of the examples presented can easily be rescaled to any other choice of dipole intensity.

Noise variance

The selection of a standard deviation for the noise is not immediately obvious, in part because of the

widespread practice of averaging experimental data. In theory, we could average the trials until the noise is reduced to any arbitrary low value. In this EEG/MEG comparison, the noise standard deviation is in units of either volts or teslas, respectively; thus, we cannot easily set a standard deviation general to both sensor types as we did with the dipole intensity.

A dipole of intensity 10 nA-m near the cerebral spinal fluid layer can generate a field that peaks roughly at 350 fT in MEG sensors, or at $4 \mu\text{V}$ in nearby EEG sensors, for the sensor patterns and model examined in this paper. In research such as that of Cuffin (1986), the standard deviation is expressed as a percentage of the peak, approximately 10%. This definition roughly translates into similar SNRs examined in Westerkamp and Aunon (1987), Stok (1987) and Achim et al. (1991). We therefore, somewhat arbitrarily, set the MEG noise standard deviation to 35 fT and the EEG noise standard deviation to $0.4 \mu\text{V}$, to reflect this 10:1 ratio. We compare with Balish et al. (1991), who had a stated noise level of 50 fT after averaging 200 trials. We note the difficulty in extracting absolute noise levels from other reports for comparison because of the widespread practice of normalizing the noise standard deviation into the field levels. As with the dipole intensity, we emphasize that all of the examples presented can easily be rescaled to any other choice of noise variance.

Sensor assumptions

In all cases, the EEG sensors are assumed to be affixed directly to the 88 mm scalp sphere, and they acquire an absolute voltage potential referenced to "infinity." In reality, EEG measurements are acquired as differential measurements with reference to a common local sensor or adjacent sensors. Here, however, we ignore this common use of a "switching" matrix. We also ignore the physical diameters of the sensors and assume that they make a point voltage measurement.

The MEG coils are placed 105 mm from the head center, representing a 17 mm offset from the scalp surface. This distance was chosen to represent the Dewar wall thickness of the larger sensor arrays and the air gap, both of which prevent the placement of the coils closer to the subject's scalp. Although these coils are often 20 mm in diameter, we also assume that they make a point magnetic field measurement and that they are oriented in the radial direction. Jeffs et al. (1987) showed that this practice is a reasonable approximation by comparing point models with integrations across the coil diameters. Since most MEG sensors are arranged in a first or second order gradiometer configuration to control external field noise, we ran a CRLB comparison between a perfect point measurement and a perfect first order gradiometer, with a coil baseline separation of 50 mm. Our CRLB results for a 37-chan-

nel comparison showed that the only differences were minor, in the deep regions of the upper hemisphere. Thus, to simplify the comparisons, we ignored any considerations of gradiometers for the MEG examples presented here.

Array patterns

The sensor array patterns presented here are identically arranged in angular separation for both the EEG and the MEG cases, and they were designed to mimic possible MEG sensor patterns because MEG sensors are much larger than EEG probes. Although EEG probes are much smaller, they, too, have practical limitations in placement, because gels may form salt bridges for electrodes spaced too closely. In the following examples, we present the error lower bounds for 127 sensors spread first over the entire upper hemisphere and then densely in one region. We then present, for comparison, the results for just 37 sensors arranged in an array pattern similar to that of commercially available 37 sensor MEG instruments. The 127 sensor dense pattern was chosen to cover the same spatial area as a 37-channel system. We also present, for comparison, the bounds of the standard EEG 10–20 array pattern, which provides a wide spatial coverage, similar to the 127 upper hemisphere pattern presented, but at a much more sparse spatial sampling.

The overall emphasis is to show which accuracies are possible for the wide spatial coverage or the dense local coverage, or the accuracy achievable with an array pattern similar to that of existing technologies or practices. Direct comparisons among different EEG and different MEG patterns are warranted, since dipole intensity and noise were held constant; however, comparisons between EEG and MEG results must consider the differences in noise assumptions and the uncertainties in model parameters. While our MEG model is relatively simple, the equivalent simple EEG model depends on many more assumptions of conductivities and sphere radii.

Upper hemisphere 127-sensor pattern results

We designed a simple pattern to cover the entire upper hemisphere without placing the sensors too close together. The first sensor is placed on the z-axis, then 6 sensors are placed evenly around a circle 15° down from the z-axis. The next ring is 30° from the z-axis, along which are 12 sensors evenly arranged. The pattern is repeated at 15° intervals for a total of 6 rings, with the rings containing 6, 12, 18, 24, 30 and 36 sensors, respectively, for a total of 127 sensors. The last ring lies completely in the x-y plane, such that the entire array provides full upper hemisphere spatial coverage. The MEG sensors are oriented radially.

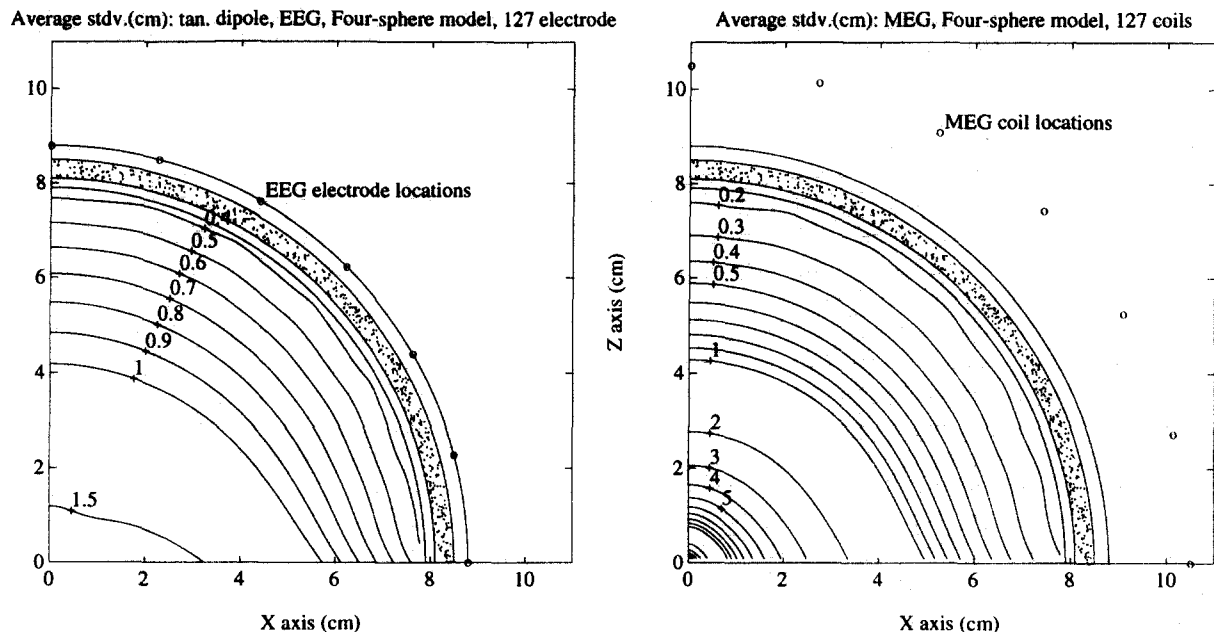


Fig. 5. Upper hemisphere 127-sensor cases for a single tangential dipole, EEG (left) and MEG (right) Cramer-Rao lower bounds. The 127-electrode pattern consists of an electrode on the z-axis and 6 concentric rings separated by 15°, consisting of 6, 12, 18, 24, 30 and 36 electrodes per ring, respectively. The 127 MEG sensors are arranged in the same angular pattern, but they are located 10.5 cm from the head origin. The contour lines are labeled with the standard deviation of the error (in cm). Linear scaling factors of $(\sigma_V/Q) = 40 \text{ V}/(\text{Am})$ and $(\sigma_B/Q) = 3.5 \times 10^{-6} \text{ T}/\text{Am}$ for the EEG and MEG cases respectively are assumed. These factors correspond to a noise standard deviation of $0.4 \mu\text{V}$ (EEG) or 35 femtoteslas (MEG) and a dipole strength (both cases) of 10 nA-m. The plots show the average of the error bound calculations for the dipole orientation stepped in 1° increments around a full circle. Both the EEG and MEG results show little sensitivity to moment orientation for this pattern and a single dipole. We emphasize that the curves can be linearly scaled for arbitrary σ/Q .

This pattern was chosen as a natural extension of commercially available 7- and 37-channel MEG sensor arrays. The sensors are spaced roughly 2 cm apart, which is about the diameter of a single MEG coil. EEG and MEG instruments are now in the design phases with roughly 100 sensors. The analysis here for 127 sensors should represent the potential accuracy of these new instruments when they are used for whole head coverage.

(1) *One tangential dipole.* In the first study, we

calculated the lower bound for a single dipole located anywhere in the positive x-z plane ($y = 0$). The dipole was stepped along at 1 mm intervals within the brain sphere. At each location, the moment angle was stepped in 1° increments from 0° to 179° , and at each angle the RMS lower bound was calculated using (18). The average RMS lower bound was calculated over all 180° , and the best and worst angles were located. At these extrema, either a minimization or a maximization algorithm was initiated to refine the estimate of the

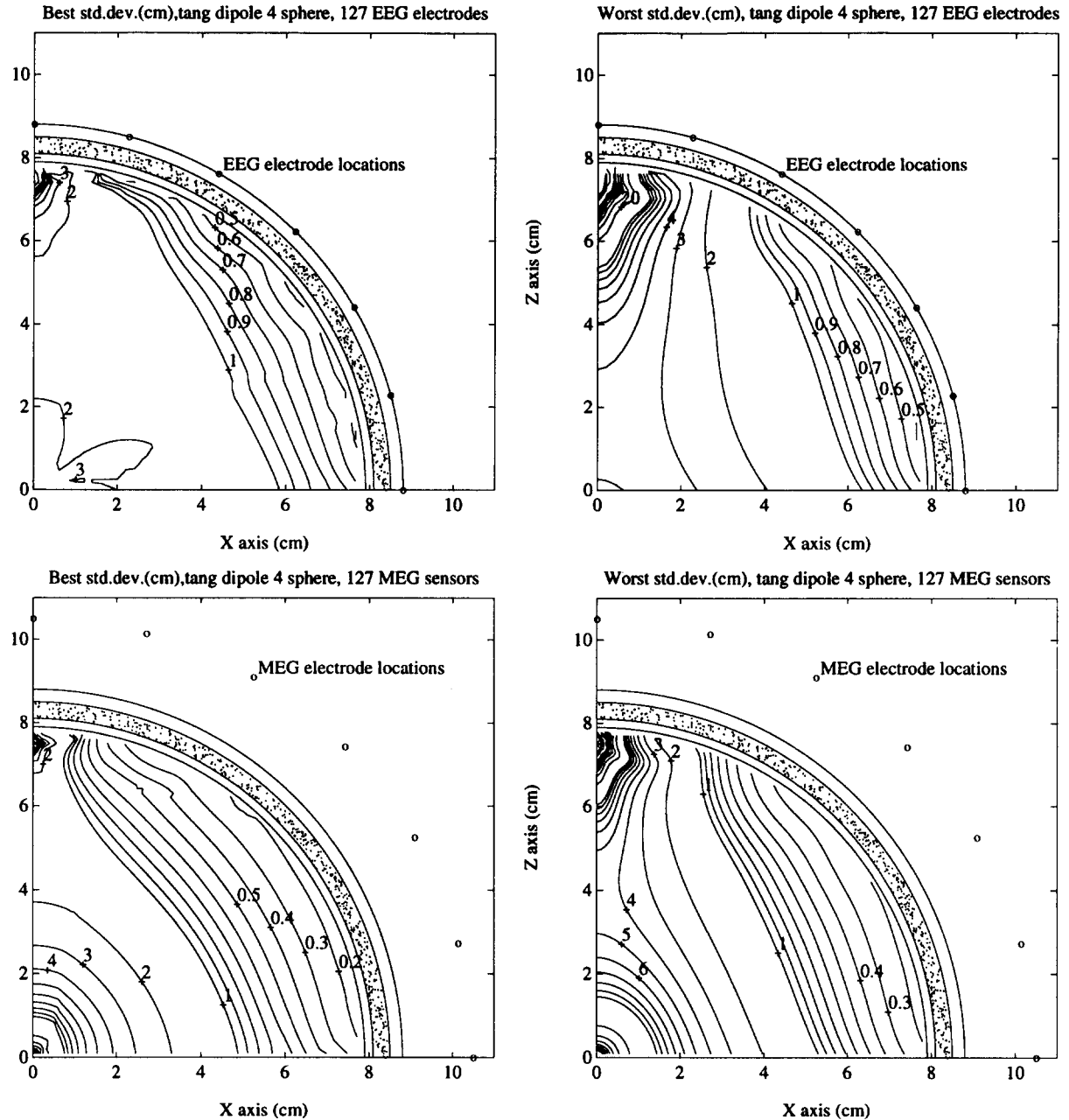


Fig. 6. Upper hemisphere 127-sensor case for two tangential dipoles, EEG (top) and MEG (bottom) Cramer-Rao lower bounds. The sensor pattern is identical to that of Fig. 5. The first dipole is at any given point in the positive x-z plane and the second is located on the z-axis at 7.5 cm. The contour level (in cm) is the RMS error bound of the first dipole because of the presence of the second dipole. Dipole intensity and noise levels are the same as in Fig. 5. The left-side figures show the CRLBs for the best possible orientation combination, and the right-side show the CRLBs for the worst.

best and the worst RMS errors, respectively. Three different bounds were retained for each location point in the grid, representing the best, average, and worst RMS errors.

In this case, the best, average, and worst bounds were similar. Fig. 5 shows the average RMS results for the EEG and MEG cases as contours representing lines of equal RMS error. For much of the upper head region, the error curves are approximately concentric. For this upper hemisphere sensor pattern, the RMS lower bounds are primarily a function of radial depth and are largely independent of orientation. Since dipole sources oriented radially produce no external magnetic field, we see an increasing MEG error as the dipole's location approaches the center. In contrast, the EEG error near the center flattens out, because this inner region is approximately equally located from all sensors. Near the surface of the sphere, both modalities exhibit similar changes in error as a function of radial depth.

(2) *Two tangential dipoles.* We now examine the rapid degradation in performance that occurs by introducing a second dipole. For simplicity in examining the effect of an additional dipole on the localization accuracy of the original dipole, we fixed the location of the second dipole on the z-axis at $z = 7.5$ cm, directly under the center of the array. Both dipoles had equal intensity Q , so all results are directly scalable to any other arbitrary intensity. By the symmetry of the location of the additional dipole on the z-axis, we can

restrict our analysis region to the positive x-z plane and infer the results for the remainder of the upper hemisphere.

As in the single dipole studies, the first dipole was stepped along on a 1 mm grid within the positive x-z plane. At each location point, the angles of *both* of the dipoles were stepped in 10° increments from 0° to 170° , resulting in a grid of 18×18 different angle combinations. For each angle pair, the RMS error bounds for the first dipole were calculated using (19). The average errors were then calculated from this 2-dimensional grid of error bounds, and the best and worst angle pairs were found. At these grid point extrema, a Nelder-Mead simplex minimization or maximization algorithm was initiated to refine the estimate of the best or worst RMS error bounds.

Fig. 6 presents the best and worst orientation results for the EEG and MEG cases. These cases, unlike that of the single dipole, have a strong dependency on dipole orientation. A wide range of error is possible between the best and worst orientation pairs. In comparison with the one dipole case above, we note that the results do not differ much along the x-axis, because the additional dipole on the z-axis is far enough away that it has little effect. As we follow along the inner radial cerebrospinal fluid layer, we see that the second dipole can affect the accuracy of the first dipole as far as 4 cm away, rapidly doubling the standard deviation error. In general, in the best moment orientation pairs, the two dipoles were pointed in orthogonal directions,

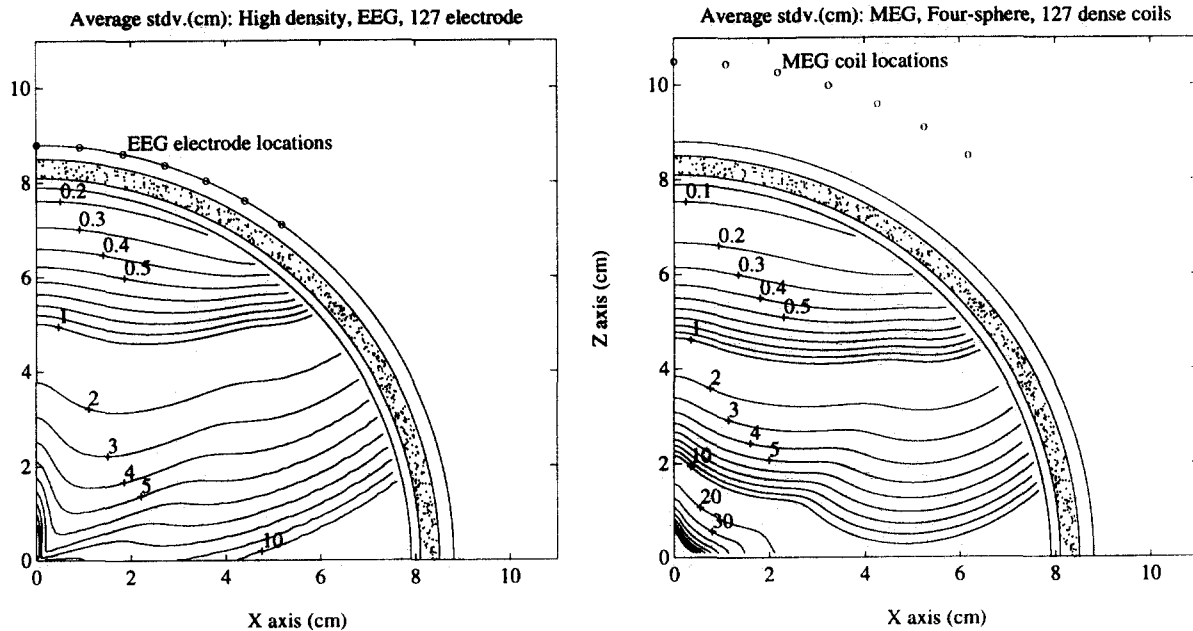


Fig. 7. Dense 127-sensor case for a single tangential dipole, EEG (left) and MEG (right) Cramer-Rao lower bounds. The array pattern is constructed as in Fig. 5 for the case of the 127-sensor upper hemisphere pattern, but is now separated by 6° , instead of 15° . Dipole intensity and noise levels are the same as in Fig. 5. The plots show the average RMS lower bound for all orientations. Increased sensitivity to moment orientation was noted near the edges of the array pattern. The increased sampling density gives better lower bounds than in Fig. 5, but only in a greatly reduced region of the head.

so their corresponding field intensities across the array were separated better than at any of the other angle combinations. The worst orientations occurred when both dipoles pointed in the same parallel direction, so that their fields had the greatest overlap.

This study has presented only a few of the endless possible combinations for two dipole intensities and positions. However, this one study shows the rapid degradation in accuracy that occurs when trying to localize two equal intensity dipoles that are relatively well situated within the array. We also see that local-

ization error is not simply a function of the relative distance between the two dipoles, but rather a complex function of absolute dipole position and orientation. We contrast this with the results in Oshiro et al. (1992). Through a limited Monte Carlo analysis Oshiro et al. (1992) erroneously claimed to show that the error is only a function of the distance between dipoles and does not depend on the orientation. While this may be true in specific instances, it is clearly not true in general. By comparing the best and worst standard deviation curves presented here, we see that their

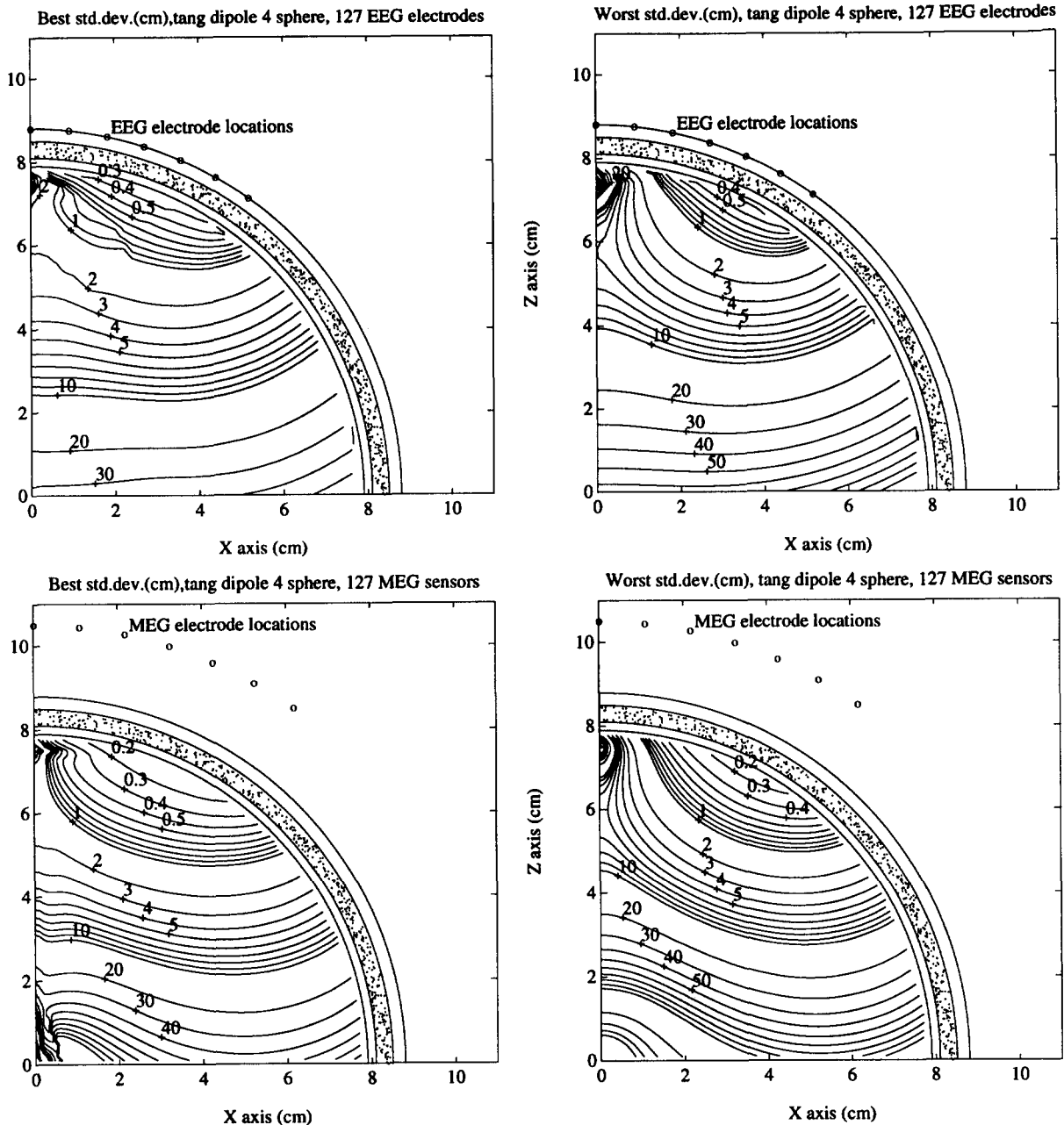


Fig. 8. Dense 127-sensor case for two tangential dipoles, EEG (top) and MEG (bottom) Cramer-Rao lower bounds. The analysis procedure was identical to that in Fig. 6, but with the sensor pattern of Fig. 7. Compared with Fig. 6, the increased sampling density does allow the two dipoles to be placed more closely together, but only in a greatly reduced region of the head.

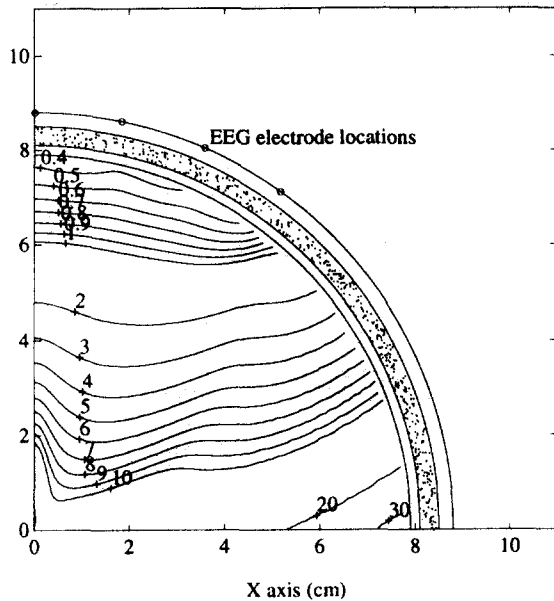
conclusion applies only to limited regions of the sphere. In general, the relative orientation between the two dipoles is very important.

Dense 127-sensor pattern results

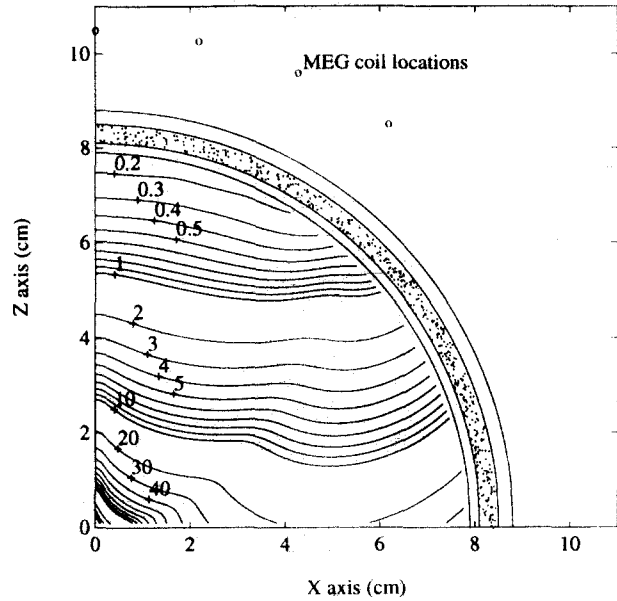
The upper hemisphere pattern examined above exhibits some variations near the inner surface of the cerebrospinal fluid, primarily because of the somewhat coarse 2 cm spacing of the sensors. Here we examine the same 127 probes, concentrated in a much smaller region, to observe more directly the effects of spatial

sampling. The array was constructed as described in the previous section, with 6 rings of sensors; however, the spacing between each of the circles and the z-axis was in 6° increments rather than 15°. The MEG sensors were oriented radially. The result was an array that subtends a 72° angle, which is of approximately the same spatial coverage as that of commercially available 37-channel MEG instruments, but with a much denser spatial sampling. Here, the spacing is, in general, less than 1 cm between sensors, which would prove to be impossible for the larger MEG coils and

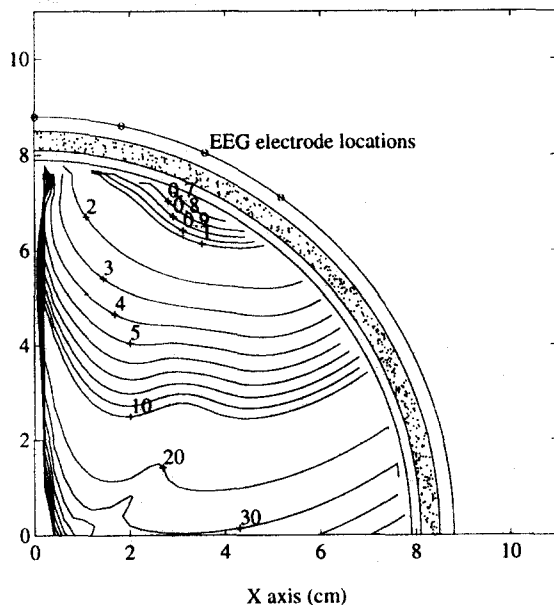
Average stdv.(cm): tan. dipole, EEG, Four-sphere model, 37 electrode



Average stdv.(cm): MEG, Four-sphere model, 37 coils



Average stdv.(cm): two dipoles, EEG, Four-sphere model, 37 electrode



Average stdv.(cm): MEG, two dipoles, Four-sphere model, 37 coils

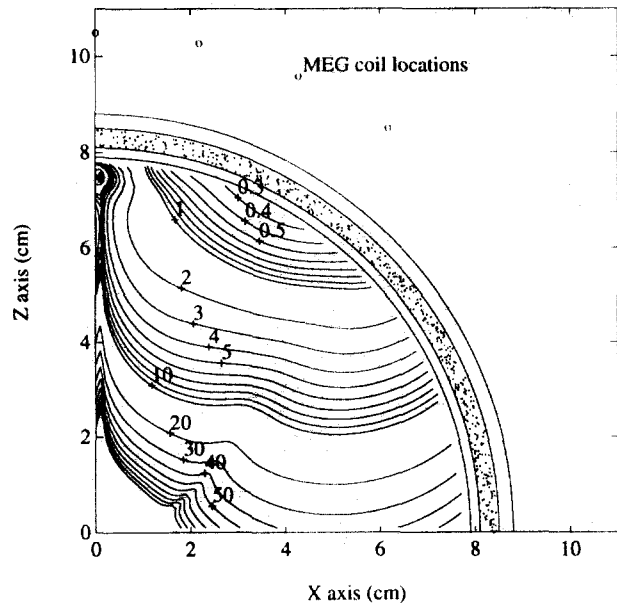


Fig. 9. The 37-sensor case with a single tangential dipole (top) or with two tangential dipoles (bottom). EEG (left) and MEG (right) CRLBs are shown for any given point in the positive x-z plane. All plots show the average RMS lower bound. The analysis procedures and scaling factors were identical to those in Figs. 5 and 6. Compared with the 127-sensor studies, the combination here of relative coarse spatial sampling and limited spatial coverage result in overall markedly poorer lower bounds.

daunting for the placement of surface EEG electrodes. Hence, this case might represent one of the densest patterns presently possible for either modality.

(1) *One tangential dipole.* The analysis procedure here was identical to that of the 127-sensor upper hemisphere pattern. Fig. 7 displays the average RMS results for the EEG and MEG cases. Here we note the immediate impact of the limited spatial coverage on overall dipole accuracy, particularly on the increased sensitivity to moment orientation caused by the array edges. Directly under the array, where array edge effects are minimized, we see an overall factor of about two improvement in the variance, relative to the upper hemisphere array, because of the increased number of sensors in the proximity of the dipole. The error bound rises rapidly in the lower regions of the sphere because of the combined effects of the squared distance to the sensor array and the poor spatial coverage of the field peaks. This latter effect is most notable on the deeper dipoles located directly on the z -axis. By offsetting the deeper dipoles from the center of the array, we are able to position the peak of the field intensity such that it falls across the array, and achieve a slightly improved lower bound.

Comparing EEG and MEG results, we see that MEG suffers more rapidly in the lower regions as a function of the three effects of depth, proximity to the sphere center, and poor spatial coverage. By comparison, EEG has a more gradually increasing error as a function of just the two effects of depth and coverage.

(2) *Two tangential dipoles.* The analysis procedure here was identical to that of the 2-dipole study for the 127 upper hemisphere pattern. Fig. 8 presents the results of the 2-dipole study for the EEG and MEG cases. The lower bounds in the deep regions and regions outside of the array have risen sharply, compared with their 1-dipole counterparts. Compared with the 2-dipole 127 upper hemisphere pattern in Fig. 6, the increased sensor density in Fig. 8 allows the two dipoles to be placed somewhat closer together, but the edge of the array confines the region with low error bounds to a relatively small area.

Thirty-seven-sensor pattern results

In this study, we arranged 3 rings of sensors, with each spaced in increments of 12° from the z -axis and each containing 6, 12, and 18 sensors, respectively, for a total of 37 sensors, as displayed in Fig. 2. The MEG sensors were oriented radially. This pattern approximates that of commercially available 37-channel MEG instruments. We note that the upper hemisphere pattern for 127 sensors has a slightly coarser spatial sampling than this 37-channel pattern (15° spacing versus 12°), but the upper hemisphere pattern covers a much wider spatial area. The dense pattern with 127 sensors has the same spatial coverage as this 37-channel instru-

ment at roughly twice the spatial sampling density (6° spacing versus 12°). Thus the 37-channel suffers in comparison with both poorer spatial coverage and spatial sampling.

(1) *One tangential dipole.* The analysis procedure for the single tangential dipole was identical to that of the 127-sensor upper hemisphere study. Fig. 9 (top) shows the average RMS EEG and MEG case for the single dipole restricted to the tangential plane. The accuracy directly under the array is comparable to that of the upper hemisphere array, but the accuracy declines much more rapidly as a function of depth. Also noticeable was a stronger dependency on dipole orientation, similar to that of the dense array above. The overall effect is a greatly reduced area directly under the array that has an accuracy comparable to that of the larger arrays.

(2) *Two tangential dipoles.* The 2-dipole analysis procedure was identical to that of the 127-sensor upper hemisphere study. Fig. 9 (bottom) shows the average RMS EEG and MEG error bounds of a dipole when an additional dipole of equal intensity was placed on the z -axis at $z = 7.5$ cm. We can see that, in almost all regions, the dipole's error bound is at least double that in the single dipole study. In the worst case, we also found that it is impossible to place two dipoles on the z -axis in the same orientation and still resolve them. This perfect array ambiguity is a consequence of the 3 perfectly symmetric rings of sensors. The general overall accuracy region is greatly reduced from that of either of the previous sensor patterns.

(3) *EEG one unconstrained dipole.* The dipole was restricted to the tangential plane in our other studies, so that comparisons could be made more readily between EEG and MEG results. In this study, we allow the EEG dipole to be unconstrained in orientation to study whether there was any significant improvement for the single dipole case. We used the same 37-sensor arrangement, and at each location point, we calculated all possible combinations of radial and tangential moment orientations in 10° increments over the range 0 – 170° . The minimization/maximization analysis was carried out in a manner identical to the 2-dipole studies above, except in this study the two angles were for the one dipole.

Fig. 10 displays the average EEG RMS error bounds for the single unconstrained dipole. In the near region of the array there was only a slight improvement of the best error bounds and a slight degradation of the worst error bounds, but on average, the results remained fairly consistent with those presented in Fig. 9. In the deeper regions, the relaxation of the tangential restriction allowed the dipole to swing into a radial direction and direct more of its surface potential across the array, thereby smoothing the error curves in these deeper regions; nonetheless, the error values are quite

comparable to the tangentially restricted dipoles. Overall, the tangential restriction allowed for simpler studies, because the moment was a function of only one angle parameter, and this restriction does not appear to have degraded the localization accuracy for the single dipole case.

EEG 10-20 sensor pattern results

Since EEG data have historically been collected in the 10-20 array pattern using 21 electrodes, we performed a study with this sensor pattern, which features wide spatial coverage and poor spatial sampling. Fig. 11 shows the average RMS results, again using the same analysis procedure as was used for the other studies. We note that a source directly underneath the sensor at approximately $x = 6$ cm and $z = 6$ cm shows no significant improvement in accuracy over radially deeper sources. Although a shallow source generates a significantly stronger signal at the surface, the spatial undersampling is such that only one nearby sensor receives a significant signal. One sensor cannot adequately locate the source, regardless of the source intensity. The deeper sources generate a signal across enough surface sensors to compensate for their relatively weaker surface signal. The overall effect of this sparse array of sensors is a relatively flat and larger

Avg stdv.(cm): tan. dipole, EEG, 4-sphere model, Ten-Twenty array

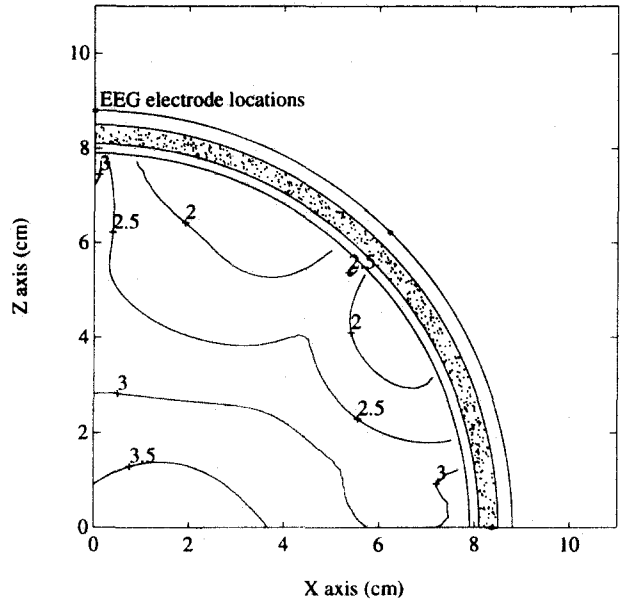


Fig. 11. EEG CRLBs for the 21 electrode arrangement for the standard 10-20 arrangement and a single tangential dipole at any given point in the positive x - z plane. The dipole intensity and EEG noise level are the same as in Fig. 5. The plot shows the average RMS lower bound for all possible dipole orientations.

lower bound error surface compared with that of the other studies.

Average stdv.(cm): free dipole, EEG, Four-sphere model, 37 electrode

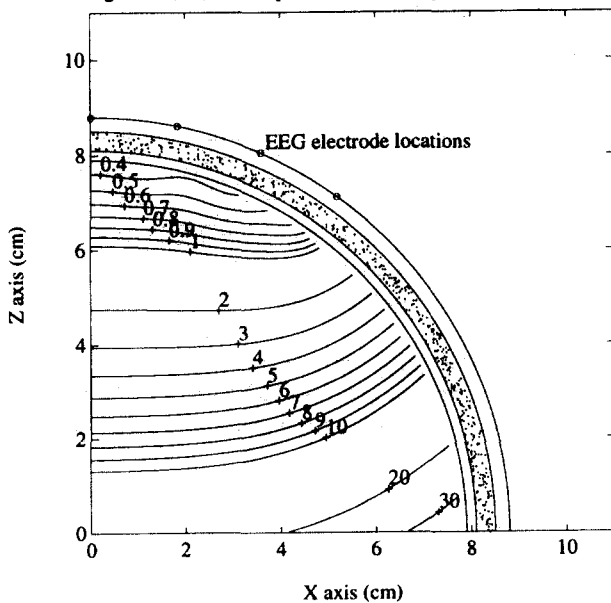


Fig. 10. EEG CRLBs for the 37-electrode case and a single freely oriented dipole (the dipole can have tangential and radial components) at any given point in the positive x - z plane. The plot shows the average RMS lower bound for all possible dipole orientations. The dipole intensity and EEG noise level are the same as in Fig. 9. The tangential restriction used in Fig. 9 (top left) has little effect on the lower bounds in the regions near the sensors; the deeper regions show relatively inconsequential shifts.

EEG and MEG fusion

The field pattern generated by a dipole across an array of EEG sensors peaks roughly along the axis of the dipole moment. In contrast, the MEG pattern peaks to the sides of the dipole moment, roughly perpendicular to the EEG pattern. In this study, we assume that both the EEG and MEG data are acquired, and we observe the improvement generated from this diversity in the information content. The sensor pattern was the same as that in the 37-sensor system, except that here we have a total of 74 measurements for the two combined sensor systems. The analysis procedure was identical to that in the other studies. Unlike the other studies, the results do *not* scale with arbitrary dipole intensity and noise variance, because both the EEG and MEG noise must be considered simultaneously. To bring the two modalities into relative scaled units, we multiplied one of the arrays by the ratio of the two noise variances, which introduces a more complex relationship between standard deviation, dipole intensity, and noise variances.

Fig. 12 shows the bound for a dipole restricted to the tangential plane. In contrast with Fig. 9 for the same array pattern and respective noise variances, we note almost no difference among the best and worst moment orientations. Since the EEG and MEG arrays complement each other so well in their field patterns,

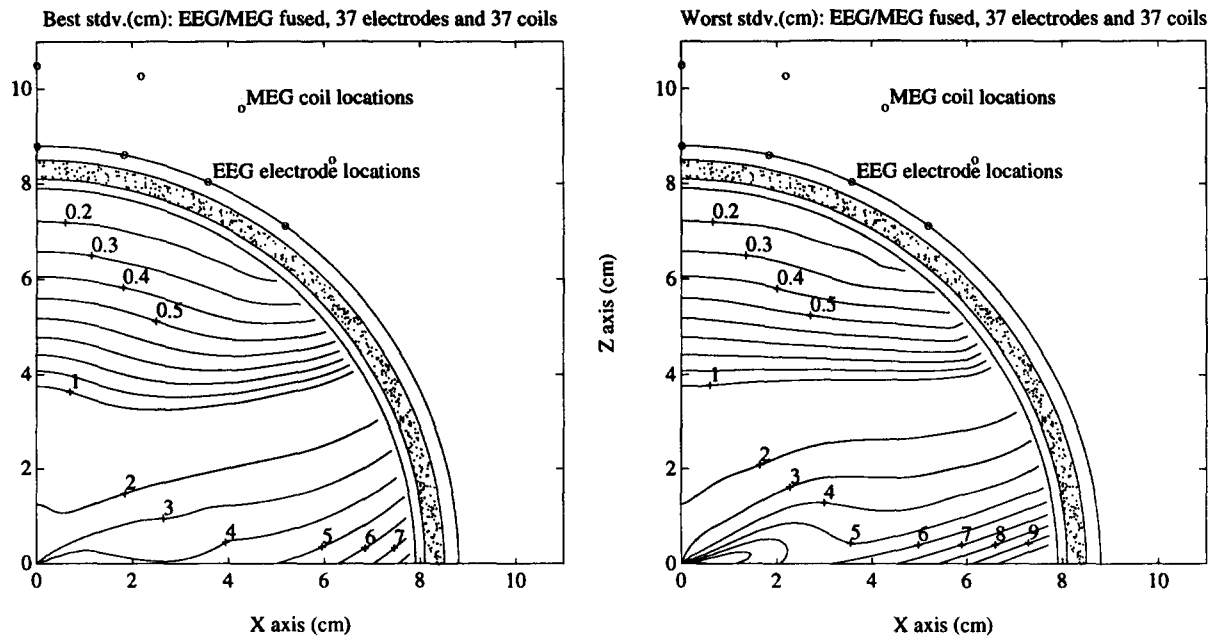


Fig. 12. Combined EEG/MEG CRLBs for the 37-electrode and 37-magnetic sensor array and a single tangential dipole at any given point in the positive x-z plane. As in the other studies, $(\sigma_V/Q) = 40 \text{ V}/(\text{Am})$, $(\sigma_B/Q) = 3.5 \times 10^{-6} \text{ T}/\text{Am}$; however, unlike all other results presented in this paper, these results do *not* scale linearly with other values of noise variance and dipole intensity. The best and worst moment orientations are presented in the left and right plots, respectively. Compared with Fig. 9 (top), notable here are the greatly improved lower bounds and the lack of any appreciable sensitivity to dipole orientation.

the dipole always points in a direction that is captured well by one of the two arrays. In the regions directly below the center of the array, an improvement occurs simply because there are twice as many measurement points. In the deeper regions, the EEG sensors have obviously improved the response near the center, and both sensor modalities have greatly improved the other deep regions.

This analysis confirms the hypotheses of Cohen and Cuffin (1983), Anogianakis et al. (1992) and Therapeutics and Technology Assessment Subcommittee (1992) concerning the potential for directly combining EEG and MEG measurements into an overall superior resolution ability, unachievable by either modality alone. One extension of this study would be to augment fixed MEG sensor arrays with a smaller array of EEG sensors to determine whether similar improvements could be obtained.

Discussion

The results presented in these exemplar studies focus on the single time slice problem, but the formulas presented for the CRLB are for the more general temporal problem. The CRLB formulas show the improvement achievable by considering multiple time slices, in which the sample spacing is large enough to decorrelate the noise. In the simplest case of the fixed

dipole moment, the standard deviations are, at a minimum, improved by the square root of the number of time slices. This effect is analogous to signal averaging over time. If the time series of the dipole moments have any algebraic independence, the results are improved further. An addition to the formulas would be the inclusion of the fixed moment dipole model, which would improve the lower bounds by incorporating the knowledge that the dipole does not “rotate”; however, the “rotating” formulas presented here are more general. The work of Baumgartner et al. (1991) and Achim et al. (1991) may have benefited from using these spatiotemporal CRLBs as a rapid analysis tool in interpreting their specific case studies of dipole locations and time series.

The RMS errors presented in this study do not consider the directional bias that could occur. In the case of EEG and MEG, with data measured from external sensors (i.e., no invasive probes), the greatest localization error will, in general, be in the radial direction, because the tangential directions are more accurately measured by the surface arrays (the “preferred directions,” as noted by Cohen and Cuffin (1983)). If we were to model the cortex as a simple thin shell beneath the skull, we might be able to ignore this radial error; the tangential errors were in general much smaller. In reality, the cortical folds (analyzed in some detail in Kaufman et al. (1991)) also force consideration of the radial location of the dipole. In the absence

of any prior information regarding the importance of one direction over another, we argue here that error in all directions is equally important.

The approaches presented here will also assist in the analysis of novel sensor locations, orientations, and parameter sensitivities by providing a preliminary CRLB baseline. We emphasize that while small CRLB bounds will not guarantee that such standard deviations will ever be achievable, large CRLB bounds will steer us clear of situations where the desired accuracy would be impossible.

We thank Chris C. Wood and the Biophysics Group at the Los Alamos National Laboratory for their early reviews and comments on the preliminary results of this study.

Appendix: Cramer-Rao derivation

In this appendix, we derive the Fisher Information Matrix and the corresponding Cramer-Rao lower bound for the general spatiotemporal model.

We define some notation and develop the bound to parallel the work of Stoica and Nehorai (1989). We define \mathbf{D} as the partials of the gain matrix \mathbf{G} :

$$\begin{aligned} \bar{\mathbf{l}}_k &\equiv [l_{xk}, l_{yk}, l_{zk}] \\ \mathbf{d}(l_{xk}) &\equiv \frac{\partial}{\partial l_{xk}} \mathbf{G}(\bar{\mathbf{l}}_k) \\ \mathbf{d}(\bar{\mathbf{l}}_k) &\equiv [\mathbf{d}(l_{xk}), \mathbf{d}(l_{yk}), \mathbf{d}(l_{zk})] \\ \mathbf{D} &\equiv [\mathbf{d}(\bar{\mathbf{l}}_1), \dots, \mathbf{d}(\bar{\mathbf{l}}_k), \dots, \mathbf{d}(\bar{\mathbf{l}}_p)] \end{aligned} \quad (20)$$

where l_{xk} refers to the x-axis component of the k^{th} dipole location, and, similarly for the other subscripts. Arrange the p moments at the j^{th} time slice, $\mathbf{q}(j)$, into a block diagonal matrix,

$$\mathbf{X}(j) \equiv \begin{bmatrix} \mathbf{I}_3 \otimes \bar{\mathbf{q}}_1(j) & & 0 \\ & \dots & \\ 0 & & \mathbf{I}_3 \otimes \bar{\mathbf{q}}_p(j) \end{bmatrix}, \quad (21)$$

where \mathbf{I}_3 is a 3×3 identity matrix and “ \otimes ” denotes the Kronecker product. (The Kronecker product of a $(p \times q)$ matrix $\mathbf{A} = \{a_{ij}\}$ and an $(m \times n)$ matrix $\mathbf{B} = \{b_{ij}\}$ is the $(pm \times qn)$ matrix, $\{a_{ij}b_{kl}\}$, denoted by $\mathbf{A} \otimes \mathbf{B}$.)

With our parameters and their partials thus redefined into the matrices \mathbf{G} , \mathbf{D} , and \mathbf{X} , we group these together into two more matrices before deriving the Fisher Information Matrix. This notation also simplifies the expressions for inverting the FIM to obtain the lower bounds:

$$\begin{aligned} \Gamma &\equiv \sum_{j=1}^n [(\mathbf{DX}(j))^T (\mathbf{DX}(j))] \\ \Delta(j) &\equiv \mathbf{G}^T \mathbf{DX}(j) \\ \Delta &\equiv [\Delta(1)^T, \dots, \Delta(n)^T]^T \end{aligned} \quad (22)$$

Thus, for m sensors, n time slices, additive zero-mean white noise with a variance ν , and the dipole moments and locations grouped as defined above, the Fisher Information Matrix is (Stoica and Nehorai 1989)

$$\mathbf{J} = \frac{1}{\nu} \begin{bmatrix} mn & 0 & 0 \\ 0 & \mathbf{I}_n \otimes \mathbf{G}^T \mathbf{G} & \Delta \\ 0 & \Delta^T & \Gamma \end{bmatrix}. \quad (23)$$

The 3 diagonal elements represent the information content of the scalar noise variance, the set of moment parameters, and the set of location parameters, respectively. The off-diagonal terms represent the cross-information between the various parameters. With this partitioning and with the use of the standard matrix inversion formulas (Sorenson 1985), we can readily invert this matrix analytically. We are particularly interested in the diagonal elements, since the Cramer-Rao lower bound for the i^{th} parameter ψ_i is simply the i^{th} diagonal element of \mathbf{J}^{-1} (Sorenson 1985).

The off-diagonal zero elements in \mathbf{J} make the lower bound for the scalar noise variance particularly easy to calculate:

$$\text{CRLB}(\nu) = \frac{2\nu^2}{mn}. \quad (24)$$

The lower bound covariance matrix for all p locations in \mathbf{l} is found in the lower $3p \times 3p$ portion of matrix \mathbf{J}^{-1} ,

$$\text{CRLB}(\mathbf{l}) = \nu \left[\Gamma - \Delta^T [\mathbf{I}_n \otimes (\mathbf{G}^T \mathbf{G})^{-1}] \Delta \right]^{-1}. \quad (25)$$

Simplifying using (22),

$$\begin{aligned} &= \nu \left[\sum_{j=1}^n (\mathbf{DX}(j))^T (\mathbf{DX}(j)) \right. \\ &\quad \left. - [(\mathbf{DX}(1))^T \mathbf{G} \dots (\mathbf{DX}(n))^T \mathbf{G}] [\mathbf{I}_n \otimes (\mathbf{G}^T \mathbf{G})^{-1}] \begin{bmatrix} \mathbf{G}^T \mathbf{DX}(1) \\ \dots \\ \mathbf{G}^T \mathbf{DX}(n) \end{bmatrix} \right]^{-1} \end{aligned} \quad (26)$$

$$= \nu \left[\sum_{j=1}^n (\mathbf{DX}(j))^T \mathbf{I} (\mathbf{DX}(j)) - \sum_{j=1}^n (\mathbf{DX}(j))^T \mathbf{G} (\mathbf{G}^T \mathbf{G})^{-1} \mathbf{G}^T \mathbf{DX}(j) \right]^{-1} \quad (27)$$

$$= \nu \left[\sum_{j=1}^n (\mathbf{DX}(j))^T [1 - \mathbf{G} (\mathbf{G}^T \mathbf{G})^{-1} \mathbf{G}^T] (\mathbf{DX}(j)) \right]^{-1} \quad (28)$$

$$= \nu \left[\sum_{j=1}^n (\mathbf{DX}(j))^T \mathbf{P}_G^\perp (\mathbf{DX}(j)) \right]^{-1} \quad (29)$$

where $\mathbf{P}_G^\perp = (\mathbf{I} - \mathbf{G} \mathbf{G}^T) = (\mathbf{I} - \mathbf{P}_G)$ is the orthogonal complement of the projection matrix for \mathbf{G} , and \mathbf{G}^\dagger is the full rank pseudoinverse of \mathbf{G} , $\mathbf{G}^\dagger = (\mathbf{G}^T \mathbf{G})^{-1} \mathbf{G}^T$.

The lower bounds for the moment series at each time slice j can be readily expressed in terms of the lower bound for the location. If we define $\gamma \equiv$

CRLB(\mathbf{l})/ ν , then the lower bound covariance matrix for each moment time slice j , $j = 1, \dots, n$ is

$$\text{CRLB}(\mathbf{q}(j)) = \nu [(\mathbf{G}^T \mathbf{G})^{-1} + \mathbf{G}^T \mathbf{D}\mathbf{X}(j) \gamma (\mathbf{G}^T \mathbf{D}\mathbf{X}(j))^{-1}]. \quad (30)$$

We can simplify these formulas for the single time slice localization case. Eq. 29 reduces to

$$\text{CRLB}(\mathbf{l}) = \nu [(\mathbf{D}\mathbf{X}(1))^T \mathbf{P}_G^+ (\mathbf{D}\mathbf{X}(1))]^{-1}. \quad (31)$$

If we assume all dipoles to be of equal intensity Q , then $\mathbf{X}(1)$ can be factored as $Q\hat{\mathbf{X}}$, where $\hat{\mathbf{X}}$ comprises just the orientations of all the dipoles, and we have dropped the single time index for convenience. Thus (31) can be factored as

$$\text{CRLB}(\mathbf{l}) = \frac{\nu}{Q^2} [(\mathbf{D}\hat{\mathbf{X}})^T \mathbf{P}_G^+ (\mathbf{D}\hat{\mathbf{X}})]^{-1}. \quad (32)$$

These formulas depend on inverting $\mathbf{G}^T \mathbf{G}$, and therefore a brief discussion about its rank is important. In the EEG and MEG cases studied in this paper, we assumed that the dipole lay in the tangential plane, i.e., that the radial component was assumed known and equal to zero. Since \mathbf{G} comprises submatrices \mathbf{G}_i for each dipole, then each \mathbf{G}_i must be appropriately expressed as a 2×2 matrix, before attempting the inverse of $\mathbf{G}^T \mathbf{G}$. If $\mathbf{G}^T \mathbf{G}$ becomes singular for a particular selection of dipoles, then the inverse is undefined, and we cannot calculate the variance. The reduced rank Moore-Penrose pseudoinverse is inappropriate here and we restrict ourselves to full-rank inverses of $\mathbf{G}^T \mathbf{G}$.

References

- Achim, A., Richer, F. and Saint-Hilaire, J.M. Methodological considerations for the evaluation of spatiotemporal source models. *Electroenceph. clin. Neurophysiol.*, 1991, 79: 227–240.
- Anogianakis, G., Badier, J.M., Barret, G. et al. A consensus statement on relative merits of EEG and MEG. Editorial. *Electroenceph. clin. Neurophysiol.*, 1992, 82: 317–319.
- Arthur, R.M. and Geselowitz, D.B. Effect of inhomogeneities on the apparent locations and magnitude of a cardiac dipole source. *IEEE Trans. Biomed. Eng.*, 1970, 17: 141–146.
- Ary, J.P., Klein, S.A. and Fender, D.H. Location of sources of evoked scalp potentials: corrections for skull and scalp thicknesses. *IEEE Trans. Biomed. Eng.*, 1981, 28: 447–452.
- Balish, M., Sato, S., Connaughton, P. and Kufra, C. Localization of implanted dipoles by magnetoencephalography. *Neurology*, 1991, 41: 1072–1076.
- Baumgartner, C., Sutherland, W.W., Di, S. and Barth, D.S. Spatiotemporal modeling of cerebral evoked magnetic fields to median nerve stimulation. *Electroenceph. clin. Neurophysiol.*, 1991, 79: 27–35.
- Brody, D.A., Terry, F.H. and Ideker, R.E. Eccentric dipole in a spherical medium: generalized expression for surface potential. *IEEE Trans. Biomed. Eng.*, 1973, 20: 141–143.
- Cohen, D. and Cuffin, B.N. Demonstrations of useful differences between magnetoencephalogram and electroencephalogram. *Electroenceph. clin. Neurophysiol.*, 1983, 56: 38–51.
- Cohen, D., Cuffin, B.N., Yunokuchi, K., Maniewski, R., Purcell, C., Cosgrove, G.R., Ives, J., Kennedy, J.G. and Schomer, D.L. MEG versus EEG localization test using implanted sources in the human brain. *Ann. Neurol.*, 1990, 28: 811–817.
- Cuffin, B.N. Effects of measurement errors and noise on MEG moving dipole inverse solutions. *IEEE Trans. Biomed. Eng.*, 1986, 33: 854–861.
- Cuffin, B.N. Effects of head shape on EEGs and MEGs. *IEEE Trans. Biomed. Eng.*, 1990, 37: 44–52.
- Cuffin, B.N. Eccentric spheres models of the head. *IEEE Trans. Biomed. Eng.*, 1991, 38: 871–878.
- Cuffin, B.N. and Cohen, D. Comparison of the magnetoencephalogram and electroencephalogram. *Electroenceph. clin. Neurophysiol.*, 1979, 47: 132–146.
- Hari, R., Hämäläinen, M., Ilmoniemi, R. and Lounasmaa, O.V. MEG versus EEG localization test. Letter to the Editor. *Ann. Neurol.*, 1991, 30: 222–223.
- Ilmoniemi, R.J., Hämäläinen, M.S. and Knuutila, J. The forward and inverse problems in the spherical model. In: H. Weinberg, G. Stroink and T. Katila (Eds.), *Biomagnetism: Applications and Theory*. Pergamon, Oxford, 1985: 278–282.
- Jeffs, B., Leahy, R. and Singh, M. An evaluation of methods for neuromagnetic image reconstruction. *IEEE Trans. Biomed. Eng.*, 1987, 34: 713–723.
- Kaufman, L., Kaufman, J.H. and Wang, J.Z. On cortical folds and neuromagnetic fields. *Electroenceph. clin. Neurophysiol.*, 1991, 79: 211–226.
- McGillem, C.D., Aunon, J.I. and Yu, K. Signals and noise in evoked brain potentials. *IEEE Trans. Biomed. Eng.*, 1985, 3: 1012–1016.
- Mosher, J.C., Lewis, P.S. and Leahy, R.M. Spatial localization of neural sources using the magnetoencephalogram. In: *Fifth ASSP Workshop on Spectrum Estimation and Modeling*, Rochester, NY, 1990: 289–293.
- Mosher, J.C., Lewis, P.S. and Leahy, R.M. Multiple dipole modeling and localization from spatio-temporal MEG data. *IEEE Trans. Biomed. Eng.*, 1992, 39: 541–557.
- Oshiro, O., Mukai, M., Takeuchi, F. and Kuriki, S. Analysis of errors in neuromagnetic localization of multiple current dipole sources. *Phys. Med. Biol.*, 1992, 37: 845–852.
- Sarvas, J. Basic mathematical and electromagnetic concepts of the biomagnetic inverse problem. *Phys. Med. Biol.*, 1987, 32: 11–22.
- Sorenson, H.W. *Parameter Estimation*. Marcel Dekker, New York, 1985.
- Snyder, A.Z. Dipole source localization in the study of EP generators: a critique. *Electroenceph. clin. Neurophysiol.*, 1991, 80: 321–325.
- Stoica, P. and Nehorai, A. MUSIC, maximum likelihood, and Cramer-Rao Bound. *IEEE Trans. Acoust. Speech Signal Proc.*, 1989, 37: 720–741.
- Stok, C.J. The influence of model parameters on EEG/MEG single dipole source estimation. *IEEE Trans. Biomed. Eng.*, 1987, 34: 289–296.
- Therapeutics and Technology Assessment Subcommittee. Assessment: magnetoencephalography (MEG). *Neurology*, 1992, 42: 1–4.
- Westerkamp, J.J. and Aunon, J.I. Optimum multielectrode a posteriori estimates of single-response evoked potentials. *IEEE Trans. Biomed. Eng.*, 1987, 34: 13–22.
- Williamson, S.J. MEG versus EEG localization test. Letter to the Editor. *Ann. Neurol.*, 1991, 30: 222.
- Wilson, F.N. and Bayley, R.H. The electric field of an eccentric dipole in a homogeneous spherical conducting medium. *Circulation*, 1950, 1: 84–92.
- Zhou, H. and Van Oosterom, A. Computation of the potential distribution in a four-layer anisotropic concentric spherical volume conductor. *IEEE Trans. Biomed. Eng.*, 1992, 39: 154–158.